Flow instability of an axial flow pump-as-turbine using relative streamline coordinates

PLEASE CITE THIS ARTICLE AS DOI: 10.1063/5.0192004

Flow instability of an axial flow pump-as-turbine using relative streamline coordinates

Kan Kan (阚阚),[1,2,a)] Qingying Zhang (张清滢),[1] Jiangang Feng (冯建刚),[3] Yuan Zheng (郑源),[1,2] Hui Xu (徐辉),[3] Mosè Rossi,[4] and Haoyu Li (李昊宇)[1]

AFFILIATIONS
[1]College of Energy and Electrical Engineering, Hohai University, Nanjing 211100, PR China
[2]College of Water Conservancy and Hydropower Engineering, Hohai University, Nanjing 210098, PR China
[3]College of Agricultural Science and Engineering, Hohai University, Nanjing 210098, PR China
[4]Department of Industrial Engineering and Mathematical Sciences (DIISM), Marche Polytechnic University, Ancona 60131, Italy
[a)]Author to whom correspondence should be addressed: kankan@hhu.edu.cn

ABSTRACT: When axial flow pumps-as-turbines (PATs) operate under off-design conditions, unstable and unsteady flow structures appear in the internal flow field, resulting in suboptimal functioning. These operating conditions not only decrease the efficiency of the hydraulic machines but also affect their mechanical reliability. This study establishes relative streamline coordinates, based on the blade's mean camber line, to investigate flow instabilities in axial flow PATs from a new perspective. Numerical simulations on an axial flow PAT were performed and validated using experimental data. The results show that flow separation is more likely to occur due to the more curved profile at the blade's suction surface, leading to considerable fluctuations in velocity along the flow direction and enstrophy amplitude near both the hub and impeller shroud. Moreover, the poor matching of the relative inflow angle of the impeller with the blade inlet angle leads to impingement losses near their leading edge, generating unstable flows and significant pressure pulsations, which induces hydraulic instability within the impeller. In addition to rotor-stator interference effects, the curvature of the blade suction surface profile and the bend structure of inlet conduit are significant factors that influence the pressure pulsation distribution of the PAT. An analysis of the enstrophy transport equation indicates that the relative vortex generation and the Reynolds stress dissipation terms play a key role in both vortex generation and dissipation, whereas the viscous term has a lower influence. These findings can serve as a reference for the optimization and efficient design of axial flow PATs.

I. INTRODUCTION

Reducing carbon emissions and increasing the proportion of renewable energy sources have become issues of global importance.[1] With the increasing demand for renewable energy, there has been considerable investment in small-scale hydropower power generation worldwide.[2,3] However, in remote and underdeveloped areas, the operating and installation costs of conventional hydraulic turbines still pose a major challenge. Considering the availability and cost advantages of commercial hydraulic pumps, the pump-as-turbine (PAT) technology has been gaining interest as an economic alternative to conventional small-size hydraulic turbines in such areas. As a result, it has become a crucial research topic in the small-scale hydropower sector worldwide.[4] In PATs, pumps essentially behave as hydraulic turbines, offering advantages such as low investment costs, simple design, and easy maintenance.[5,6] The prototype impeller of a PAT has been designed based on the pump theory, resulting in a blade inlet angle that does not match with the original flow passage components when the pump operates in the turbine mode.[7] This often leads to a lower efficiency in reverse mode operation compared to the direct one. In addition, the absence of flow regulation components, such as movable guide vanes, limits the range of high-efficiency operation.[8] When operating under off-design conditions, the internal flow field within the PAT exhibits flow separation, wakes, secondary flows, and other unstable flow phenomena that affect its operation stability.[9,10] In particular, the hydraulic instability leads to severe mechanical vibrations that are amplified when the PAT deviates from the design conditions. Therefore, studying flow instability problems of the PAT is crucial to addressing this issue as it helps prevent failures and ensures the secure and stable operation of hydraulic machines.

In previous studies on PAT technology, researchers primarily focused on predicting the performance of PATs. Several performance prediction models have been developed through theoretical derivation, experimental verification[9,11] and artificial neural network.[12,13] However, the general application of PAT performance conversion theory in these studies was poor, and there was a large difference between the prediction and experimental results, while a few studies[11-13] could accurately predict PAT performance. With the development of computational fluid dynamics (CFD), numerical simulations have become essential for studying the hydraulic characteristics of PATs. Nasir et al.[14] performed numerical simulations on a centrifugal PAT. The numerical results were validated using experimental data, indicating good agreement (with error percentages lower than 3%). Yang et al.[15] numerically simulated a large vaned-voluted centrifugal pump to evaluate its performance in the pump and turbine modes. The results showed that the best efficiency point (BEP) of this centrifugal PAT presented a higher flow-rate and head compared to the direct mode. Lin et al.[16] presented a theoretical method to predict the optimum efficiency point of PATs within a specific speed range, using the impeller-volute matching principle. As a result, the proposed method could forecast the BEP with an error of less than 5%.

Many scholars have conducted various studies on the internal flow field of PATs, investigating the influence of geometric parameters on hydraulic performance and optimizing certain parameters to enhance efficiency. Yang et al.[17] discussed the influence of blade thickness on the efficiency and hydraulic loss of a PAT and found out that an increase in blade thickness leads to a decrease in efficiency and an increase in energy losses within the impeller. Xu et al.[18] optimized the geometric design parameters of impeller blades to effectively improve the efficiency of a PAT by reducing pressure pulsations and expand the operating range of the PAT. Binama et al.[19] numerically analyzed the influence of the blade TE position on the pressure field of a centrifugal PAT and found that adjusting the TE position reduced the pulsation phenomenon of the PAT. Wang et al.[20] found out that forward-curved blades could significantly enhance the performance of a PAT. Xiang et al.[21] designed a forward-curved impeller of the PAT and found that the forward-curved blade can also significantly reduce pressure pulsation. Adu et al.[22] numerically investigated the transient characteristics of a centrifugal PAT operating at different rotational speeds, revealing that the turbulent kinetic energy and vortices of the PAT increased with increasing rotational speed. Xin et al.[23] investigated the distribution of hydraulic losses in a centrifugal PAT by entropy production theory and found that impingement, backflow, and vortices were the main hydraulic factors responsible for the irreversible hydraulic losses of the PAT. Si et al.[24] focused on an ultra-low specific speed centrifugal PAT and studied the energy conversion ability of the impeller, conducting an in-depth analysis of the unstable flow structures within the impeller and the reasons for their generation. In addition, Hu et al.[25] examined the performance variations and internal flows of a centrifugal PAT at variable rotational speeds. Their results indicated that rotational speed had a significant effect on the hydraulic performance and operational stability of the PAT. Yin et al.[26] presented a numerical method capable of efficiently simulating the unsteady flow field during the runaway process of a prototype PAT. Their results showed that the instability of the turbine's S zone was caused by vortices in the inlet section of the runner, leading to severe periodic blockage of the flow in the runner channel.

Thus far, existing research on PATs has primarily focused on the effect of impeller geometric parameters, hydraulic performance, and energy losses. To the best of the authors' knowledge, there have been few in-depth analyses of the complex flow developing inside hydraulic machines. Therefore, this study aims to establish an ideal streamline coordinate system based on the blade's mean camber line, which can reflect the hydraulic performance of the impeller within an axial flow PAT from the flow, radial, and circumferential directions. In particular, flow instability problems of the axial flow PAT are investigated to provide valuable insights for ensuring its secure and stable operation.

The rest of this paper is organized as follows. The geometric model and numerical methods are introduced in Section II. The results of this study are presented in Section III, including a discussion on the hydraulic performance of the axial flow PAT and an analysis of flow instability in the internal flow field based on the relative streamline coordinate system. Finally, conclusions are presented in Section IV.

II. NUMERICAL MODEL AND METHOD

A. Governing equations

Considering the incompressible flow in this paper, the continuity and momentum equations[27] are presented in Eqs. (1) and (2) as follows

$$\frac{\partial \overline{u}_i}{\partial x_i}=0, \tag{1}$$

$$\frac{\partial \overline{u}_i}{\partial t}+\overline{u}_j\frac{\partial \overline{u}_i}{\partial x_j}=-\frac{1}{\rho}\frac{\partial \overline{p}}{\partial x_i}+\frac{1}{\rho}\frac{\partial}{\partial x_j}\left(\mu\frac{\partial \overline{u}_i}{\partial x_j}-\rho\overline{u_i'u_j'}\right)+\overline{f}_i, \tag{2}$$

where ρ is the density; t is the physical time; x_i and x_j denote the Cartesian coordinate components in the i and j directions, respectively; $\overline{u}_i$ and $\overline{u}_j$ denote the corresponding components of the Reynolds-averaged velocity; $\overline{p}$ is the Reynolds-averaged pressure; μ is the dynamic viscosity; $\rho\overline{u_i'u_j'}$ is the Reynolds stress and $\overline{f}_i$ is the Reynolds-averaged body force.

B. Turbulence model

The k and ω equations are written as

$$\frac{\partial(\rho k)}{\partial t}+\frac{\partial}{\partial x_j}(\rho\overline{u}_j k)=\frac{\partial}{\partial x_j}\left[\left(\mu+\frac{\mu_t}{\sigma_k}\right)\frac{\partial k}{\partial x_j}\right]+P_k-\beta^*\rho k\omega \tag{3}$$

$$\frac{\partial(\rho\omega)}{\partial t}+\frac{\partial}{\partial x_j}(\rho\overline{u}_j\omega)=\frac{\partial}{\partial x_j}\left[\left(\mu+\frac{\mu_t}{\sigma_\omega}\right)\frac{\partial\omega}{\partial x_j}\right]+\alpha\frac{\omega}{k}P_k-\beta\rho\omega^2+2\rho(1-F_1)\frac{\sigma_{\omega 2}}{\omega}\frac{\partial k}{\partial x_j}\frac{\partial\omega}{\partial x_j} \tag{4}$$

The turbulent viscosity μ_t is expressed as

$$\mu_t = \frac{a_1 k \rho}{\max(a_1\omega, SF_2)} \tag{5}$$

F_1 and F_2 is calculated as

$$F_1 = \tanh\left\{\left\{\min\left[\max\left(\frac{\sqrt{k}}{\beta^*\omega y}, \frac{500\mu}{\rho y^2\omega}\right), \frac{4\rho\sigma_{\omega 2}k}{CD_{k\omega}y^2}\right]\right\}^4\right\} \tag{6}$$

$$CD_{k\omega} = \max\left(2\rho\frac{\sigma_{\omega 2}}{\omega}\frac{\partial k}{\partial x_j}\frac{\partial \omega}{\partial x_j}, 10^{-10}\right) \tag{7}$$

$$F_2 = \tanh\left\{\left[\max\left(\frac{2\sqrt{k}}{\beta^*\omega y}, \frac{500\mu}{\rho y^2\omega}\right)\right]^2\right\} \tag{8}$$

where k is the turbulent kinetic energy, ω is the turbulent frequency, P_k is the production of turbulence kinetic energy, S denotes the mean rate of the strain tensor, and y is the distance from the wall. The constants are as follows: $a_1 = 0.31$, $\beta^* = 0.09$, $\beta = 0.075$, $\sigma_k = 1.176$, $\sigma_\omega = 2$, and $\sigma_{\omega 2} = 0.856$.[28,29]

C. Geometric model

The subject of this study is an axial flow PAT model, the drawing of which is shown in Fig. 1. The geometric model is composed of four parts, namely the inlet conduit, guide vane, impeller, and outlet conduit. The basic parameters of the PAT are presented in Table I.

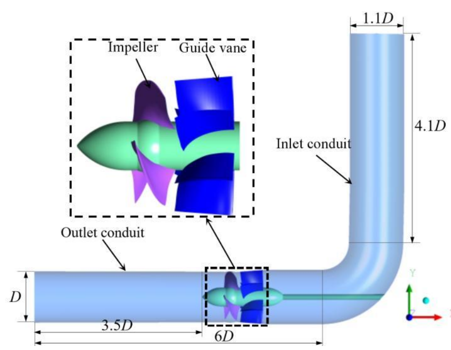

FIG. 1 Geometric model of the PAT.

TABLE I. Parameters of the PAT.

Parameter	Value
Design flow rate Q (L/s)	396.94
Design head H (m)	4.91
Rotational speed n (r/min)	1450
Number of impeller blades	3
Number of guide vane blades	6
Impeller diameter D (mm)	299.2

D. Mesh generation

The ICEM software is used to create a hexahedral structured grid for the entire computational domain. To achieve an accurate resolution of the grid distribution in the boundary layer around the blades, an O-type topology is adopted surrounding the blades. Grids near the walls are also refined to capture small-scale flow structures in these areas. The grid independence is verified using the Richardson extrapolation method.[30-32] Three sets of grids are designed, ranging from coarse to fine, with grid numbers of 4.1 million, 9.1 million, and 19.9 million, respectively. For these three sets of grids, the optimum operating condition of the PAT is simulated, and torque and efficiency are selected as evaluation parameters for the grid independence study. The grid convergence index (GCI) results are listed in Table II. Taking both torque and efficiency into consideration, as mentioned earlier, the GCI values are found to be 0.11% and 0.38%, respectively. Both these values are lower than 1%, thus, meeting the grid convergence standard.[33] The number of grids is eventually determined as 9.1 million. Fig. 2 shows the mesh of the pump section and local refinement of the impeller blade.

TABLE II. Mesh independence study.

Parameter	$\Phi = \eta$ (%)	$\Phi = T$ (N·m)
N_1	19886600	
N_2	9092056	
N_3	4092919	
Mesh refinement factor r_{21}	1.30	
Mesh refinement factor r_{32}	1.30	
Numerical value φ_1	85.70150254	182.42646
Numerical value φ_2	85.69843456	182.09172
Numerical value φ_3	85.61868887	181.81577
Extrapolated value φ_{ext}	85.3617362	181.6503352
Relative error e_a	0.09%	0.15%
Extrapolated error e_{ext}	0.3%	0.09%
Grid convergence index GCI_{fine}	0.38%	0.11%

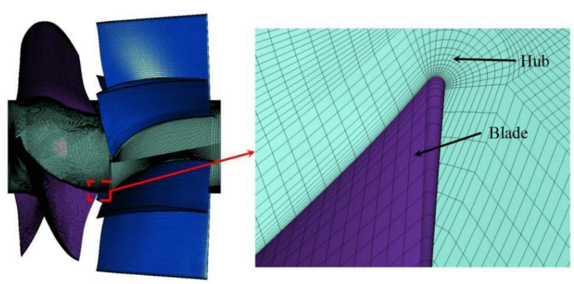

(a) (b)

FIG. 2. Mesh details of the PAT: (a) impeller and guide vane domain; (b) near blade.

F. Numerical settings

In this study, the SST k-ω turbulence model was chosen to better account for turbulent effects.[34,35] The finite volume method was used for spatial discretization, and the SIMPLEC algorithm was applied to achieve a coupled pressure-velocity solution. The pressure inlet was adopted as the inlet boundary condition, while the outlet boundary condition was set to the pressure outlet. The impeller was set in a rotating reference frame, whereas the remaining domains were set to be stationary.[36] For the interface between the impeller and stationary components, the frozen rotor approach was employed in the steady-state simulations, while the transient rotor-stator approach was used in the transient simulations. The steady-state simulations were used as initial data for the transient simulations, and the time step was set to 1.15×10^{-4} s, corresponding to 1/360 of the impeller rotation period. All wall surfaces were set as no-slip walls. Numerical simulations were considered to have converged when the residual was below 10^{-5}.

III. RESULTS AND ANALYSIS

A. CFD validation

Fig. 3 presents a comparison of the macroscopic performance of the axial flow PAT obtained numerically and experimentally. It is evident that the simulation results agree with the experimental data, with a maximum relative difference of less than 3%, particularly near the Q_{BEP} (indicated by the blue circle in Fig. 3). This demonstrates the credibility of the chosen mesh arrangement and numerical method, ensuring the precision of the numerical simulations. The operating conditions deviate further from the optimum condition, the decrease in efficiency becomes more pronounced. It is important to note the inefficiency of the PAT under off-design operating conditions.

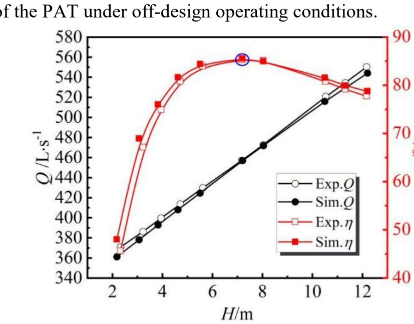

FIG. 3. Comparison between the experimental and simulation results.

B. Relative streamline coordinate system based on mean camber line of blade

The ideal impeller is assumed to be composed of an infinite number of extremely thin blades, which allows for the consideration that the water flow in the impeller is uniform and axisymmetric, and its relative motion track coincides with the blade's mean camber line. To reflect the flow characteristics along the ideal streamline direction, this study establishes a relative streamline coordinate system based on the blade's mean camber line for the impeller. This system includes three directions: the flow direction $\boldsymbol{\lambda}$, the circumferential direction $\boldsymbol{c}$, and the radial direction $\boldsymbol{r}$. Fig. 4(a) defines the length coefficient λ of the blade's mean camber line, and the flow direction is from the LE to the TE of the blades. A value of $\lambda = 0$ corresponds to the LE of the blades and a value of $\lambda = 1$ corresponds to the TE of the blades. Fig. 4(b) shows the monitoring point scheme on the blade's mean camber line for the impeller. Eleven locations are selected along the ideal flow direction, marked from 0 to 1 from the blade inlet to the outlet. Three locations are selected in the circumferential direction from the suction surface (SS) to the pressure surface (PS), marked as S, M, and P. The span indicates the location of the circumferential unfolding surface in the impeller region, span=0 for the circumferential unfolding surface at the hub, and span=1 for the circumferential unfolding surface at the shroud. In the radial direction, three spans are selected from the impeller hub to the shroud, marked as span 0.1, span 0.5, and span 0.9. Fig. 5 shows these monitoring points in the relative streamline coordinate system.

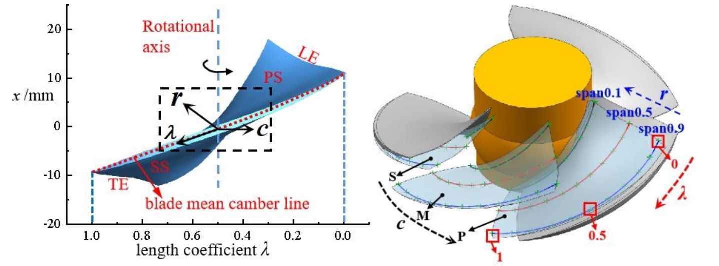

(a) (b)

FIG. 4. Relative streamline coordinate system based on blade mean camber line: (a) length coefficient of the blade's mean camber line; (b) monitoring point scheme on the blade's mean camber line.

C. Analysis of the velocity based on the streamline coordinate system

The distribution of relative velocity along the flow direction is shown in Fig. 5. According to the velocity triangle, at $0.8Q_{\mathrm{BEP}}$, the impeller inflow strikes the suction surface when it enters the LE of the blade due to the low axial velocity. In contrast, at $1.2Q_{\mathrm{BEP}}$ the impeller inflow strikes the pressure surface when it enters the LE of the blade, resulting in an impact loss. Moreover, at $0.8Q_{\mathrm{BEP}}$, the relative velocity decreases near the LE of the blade on both the suction and pressure surfaces. Under the optimum condition, the relative velocity near the LE of the blade gradually increases along the flow direction, indicating that the relative inflow angle is in good agreement with the blade inlet angle. At $1.2Q_{\mathrm{BEP}}$, it is evident that the relative velocity drops sharply at $\lambda = 0.3$. Under all operating conditions, the relative velocity near the suction surface decreases in the TE region, demonstrating that water flow in this region is obstructed. The relative velocity near the pressure surface and the middle position of the flow channel tends to increase along the flow direction, which is more consistent with the theoretical situation compared to that the near suction surface.

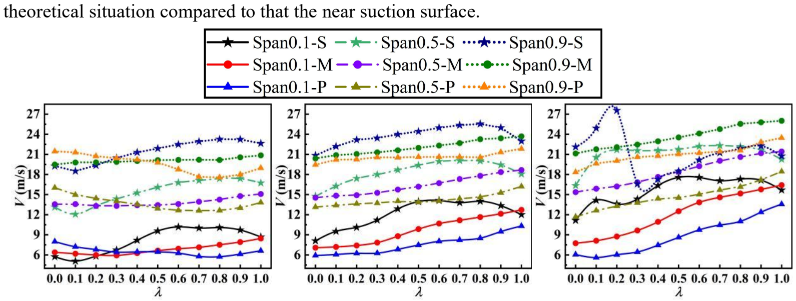

(a) (b) (c)

FIG. 5. Distribution of the relative velocity on an ideal streamline: (a) $0.8Q_{\mathrm{BEP}}$; (b) Q_{BEP}; (c) $1.2Q_{\mathrm{BEP}}$.

In axial flow machinery, it is common to assume cylindrical layer independence, and the velocity in the radial direction (V_r) is zero. Consequently, the radial velocity component can be considered as an indicator when investigating the flow instability of the PAT. Fig. 6 depicts the distribution of the radial component along the flow direction under different operating conditions. Notably, the radial velocity near the blade suction surface experiences significant fluctuations along the flow direction compared to other positions. Furthermore, compared to the pressure surface, flow separation is more likely to occur near the suction surface as the profile at the suction surface is more curved, particularly near the impeller hub, leading to significant fluctuations in the velocity distribution along the flow direction.

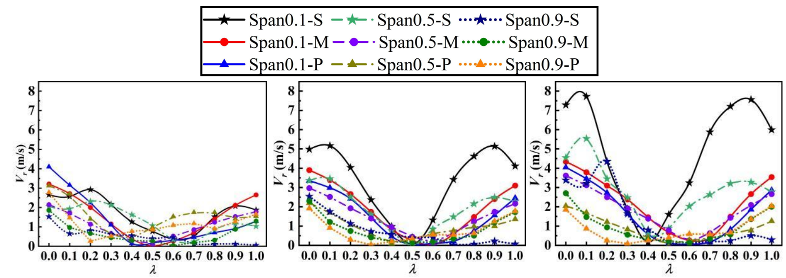

(a) (b) (c)

FIG. 6. Distribution of the radial velocity on an ideal streamline: (a) $0.8Q_{\mathrm{BEP}}$; (b) Q_{BEP}; (c) $1.2Q_{\mathrm{BEP}}$.

D. Enstrophy analysis based on the streamline coordinate system

Under off-design working conditions, the water flow hits the blade inlet edge and forms vortices that constitute an unstable flow. To accurately quantify the vortex evolution process, this study uses enstrophy to measure vortex intensity. Enstrophy is defined as the scalar $\omega^2/2$, where ω denotes the vorticity.[37]

Fig. 7 illustrates the distribution of enstrophy $\omega^2/2$ along the blade's mean camber line for the impeller under different operating conditions. According to the figure, the enstrophy has a larger value near the suction surface, indicating that an unstable flow is more likely to occur near the suction surface. At $0.8Q_{\mathrm{BEP}}$ and Q_{BEP}, the maximum enstrophy in the flow direction is concentrated at the TE of the blades. Under optimum condition, the maximum value of the enstrophy is most significant near the hub and decreases gradually along the radial direction from the impeller hub to the shroud. The greater curvature of the suction surface profiles leads to stronger vortices in the TE region of the blade. At $1.2Q_{\mathrm{BEP}}$, the maximum enstrophy in the flow direction is observed at λ = 0.3 near the impeller shroud. Fig. 8 illustrates the radial enstrophy distribution along the blade's mean camber line for the impeller under different operating conditions. The trend and distribution of enstrophy and radial enstrophy in the flow direction are generally consistent. As the flow rate increases, the percentage of radial enstrophy in total enstrophy gradually decreases.

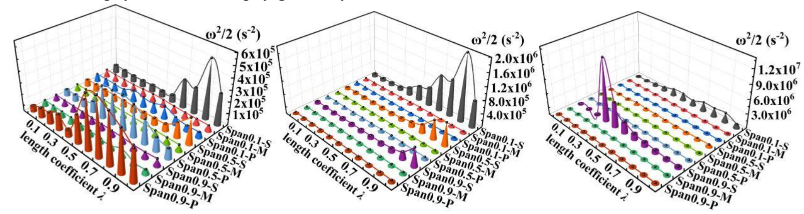

(a) (b) (c)

FIG. 7. Distribution of enstrophy on an ideal streamline: (a) $0.8Q_{\mathrm{BEP}}$; (b) Q_{BEP}; (c) $1.2Q_{\mathrm{BEP}}$.

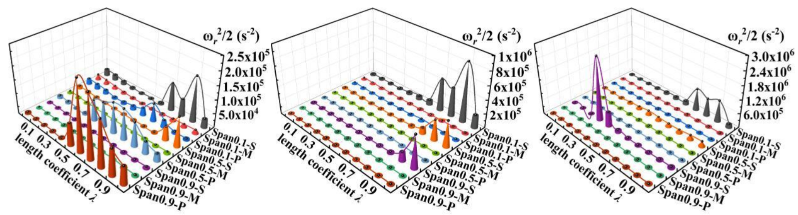

(a) (b) (c)

FIG. 8. Distribution of radial enstrophy on an ideal streamline: (a) $0.8Q_{\mathrm{BEP}}$; (b) Q_{BEP}; (c) $1.2Q_{\mathrm{BEP}}$.

E. Frequency domain analysis of the pressure pulsation

Unstable flow structures in a flow field causes pressure pulsations. To investigate the flow characteristics within the flow field of the PAT, this study uses the fast Fourier transform (FFT) method to analyze the frequency domain characteristics of the pressure values at the monitoring points on the blade mean camber line of the impeller. F_n represents the rotation frequency of the impeller. The horizontal coordinate in Fig. 9 scales the frequency dimensionless and represents the integral multiple of the impeller rotation frequency. The vertical coordinate represents the pressure coefficient, which is defined as

$$C_p = \frac{(P_i - P_{\mathrm{ave}})}{0.5\rho u_{tip}^{\ 2}} \tag{9}$$

where P_i is the transient pressure, P_{ave} is the average pressure over a time period, and u_{tip} represents the circumferential velocity of the impeller blade tip.[38] The obtained frequency domain results of pressure pulsation are presented in Fig. 9. The static and dynamic interfaces of CFX calculations are designed according to the transient rotor-stator approach, so the monitoring points follow the overall movement of the impeller, and the guide vanes rotate relative to the monitoring points. Thus, a large amplitude of C_p can be observed at the guide vane passing frequency of $6f_n$. This demonstrates that the rotor-stator interference between the guide vane and the impeller is a significant cause of pressure pulsations in the internal flow field. Additionally, due to curved inlet conduit in this model, there are also large C_p amplitudes at $1f_n$ and its multiples, specifically at $2f_n$, $3f_n$, and $4f_n$. Fig. 10 shows the distribution of the main frequency amplitude of pressure pulsation along the flow direction. In a single-impeller channel, the pressure pulsation in the middle of the flow channel is the smallest and the dominant frequency amplitude of pressure pulsation is more evenly distributed in the flow direction. At $0.8Q_{\mathrm{BEP}}$, pressure pulsation near the pressure surface is more intense, especially at the LE of the blade. In contrast, at $1.2Q_{\mathrm{BEP}}$, the pressure pulsation amplitude near the suction surface is more intense, and the maximum amplitude of pressure pulsation along the flow direction is at $\lambda = 0.3$. Compared to other conditions, the optimum condition exhibits a better inflow condition and lower pressure pulsation, and the largest pressure pulsation in the flow direction is concentrated near the LE of the blade.

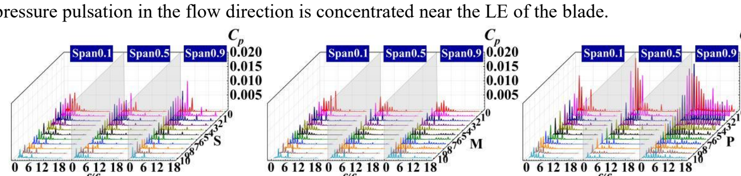

(a)

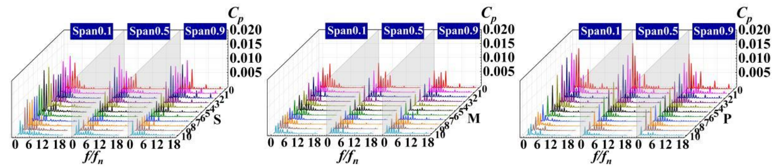

(b)

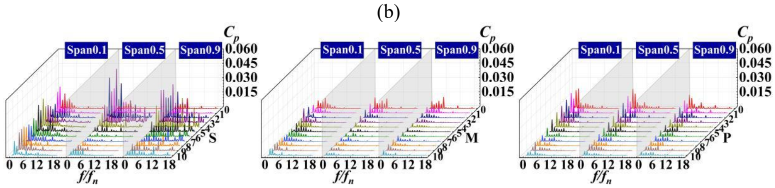

(c)

FIG. 9. Pressure pulsation frequency domain: (a) 0.8Q_{BEP}; (b) Q_{BEP}; (c) 1.2Q_{BEP}.

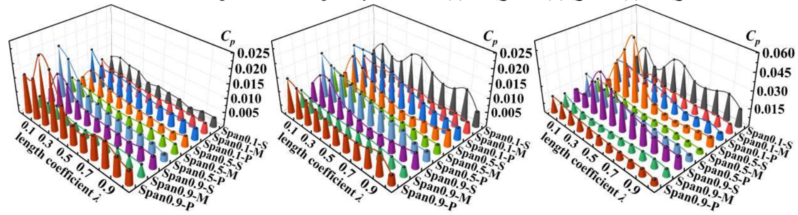

(a) (b) (c)

FIG. 10. Pressure fluctuation amplitude of the dominant frequency: (a) 0.8Q_{BEP}; (b) Q_{BEP}; (c) 1.2Q_{BEP}.

Fig. 11 shows the distribution of the pressure coefficient under different operating conditions. At 0.8Q_{BEP}, the impeller inlet flow impinges on the suction surface at the blade inlet edge of the blade, resulting in a local high-pressure region near the blade's LE. At 1.2Q_{BEP}, the impeller inlet flow at the blade inlet edge impacts the pressure surface of the blade, leading to impact loss, which hinders smooth water flow. Under the optimum operating conditions, the relative inflow angle of the blade inlet matches the blade inlet angle. Thus, the pressure distribution at the LE of the pressure and suction surfaces is relatively uniform, and the impeller inflow impingement loss is minimized. At low flow rates and under optimum conditions, localized low pressure exists near the blade's TE of the suction surface, where flow separation occurs in the TE region, thus generating a vortex flow.

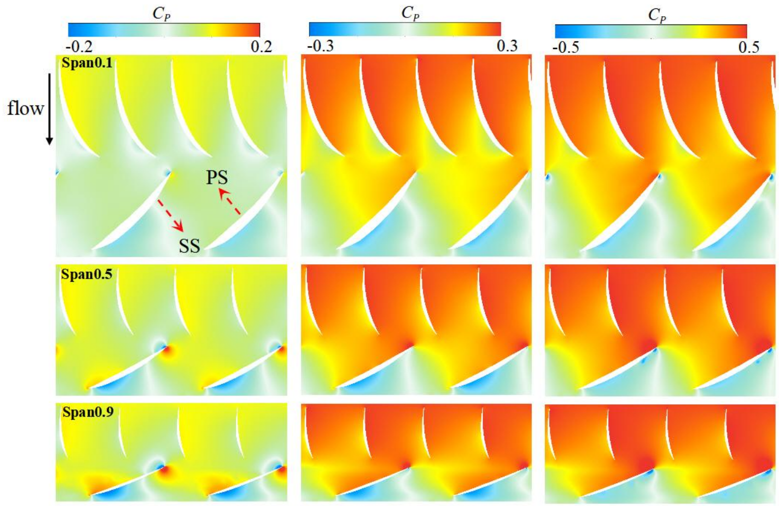

(a) (b) (c)

FIG. 11. Pressure coefficient distribution on blade-to-blade surfaces: (a) $0.8Q_{\mathrm{BEP}}$; (b) Q_{BEP}; (c) $1.2Q_{\mathrm{BEP}}$.

F. Frequency domain analysis of Reynolds-averaged enstrophy transport equation

To further analyze the unstable flow structures, the generation and development of vortices are studied using the enstrophy transport equation. Many previous studies employed transport equations derived from direct numerical simulations and did not consider the effect of the Reynolds stress, which renders them inapplicable to the analysis conducted under the Reynolds-averaged Navier-Stokes (RANS) method. In this study, the Reynolds-averaged enstrophy transport equation is derived on the basis of RANS equations. Eq. (2) can be written as follows[34]

$$\frac{\partial \bar{u}_i}{\partial t}+\bar{u}_j\frac{\partial \bar{u}_i}{\partial x_j}=\frac{1}{\rho}\frac{\partial}{\partial x_j}\left(-\delta_{ij}\bar{p}+2\mu\bar{S}_{ij}-\rho\overline{u_i'u_j'}\right)+\bar{f}_i \tag{10}$$

$\rho\overline{u_i'u_j'}$ can be expressed as

$$-\rho\overline{u_i'u_j'}=2\mu_t\bar{S}_{ij}-\frac{2}{3}\delta_{ij}\rho k \tag{11}$$

where $\bar{S}_{ij}$ is the mean strain tensor, and δ_{ij} is Kronecker delta.[39] By substituting the Reynolds stress formula into the RANS equation, Eq. (10) can be written in the vector form as

$$\frac{\partial\bar{\boldsymbol{u}}}{\partial t}+\left(\bar{\boldsymbol{u}}\cdot\nabla\right)\bar{\boldsymbol{u}}=-\frac{1}{\rho}\nabla\bar{p}+\nu\nabla^2\bar{\boldsymbol{u}}+\nu_t\nabla^2\bar{\boldsymbol{u}}-\frac{2}{3}\nabla k+\bar{\boldsymbol{f}} \tag{12}$$

where $\bar{\boldsymbol{u}}$ is the Reynolds-averaged velocity vector, ν is the kinematic viscosity, ν_t is the eddy viscosity, ∇ is the Hamiltonian operator, $\bar{\boldsymbol{f}}=-2(\bar{\boldsymbol{c}}\times\bar{\boldsymbol{u}})$, and $\bar{\boldsymbol{c}}$ is the Reynolds-averaged angular velocity. According to the vector equation,

$$\nabla\left(\frac{\bar{\boldsymbol{u}}^2}{2}\right)=\left(\bar{\boldsymbol{u}}\cdot\nabla\right)\bar{\boldsymbol{u}}+\bar{\boldsymbol{u}}\times\left(\nabla\times\bar{\boldsymbol{u}}\right) \tag{13}$$

Eq. (12) can be then rewritten as:

$$\frac{\partial\bar{\boldsymbol{u}}}{\partial t}+\nabla\left(\frac{\bar{\boldsymbol{u}}^2}{2}\right)-\bar{\boldsymbol{u}}\times\bar{\boldsymbol{\omega}}=-\frac{1}{\rho}\nabla\bar{p}+\nu\nabla^2\bar{\boldsymbol{u}}+\nu_t\nabla^2\bar{\boldsymbol{u}}-\frac{2}{3}\nabla k-2\left(\boldsymbol{c}\times\bar{\boldsymbol{u}}\right) \tag{14}$$

Taking the curl of Eq. (14), the following is obtained:

$$\frac{\partial\bar{\boldsymbol{\omega}}}{\partial t}-\left(\bar{\boldsymbol{\omega}}\cdot\nabla\right)\bar{\boldsymbol{u}}+\left(\bar{\boldsymbol{u}}\cdot\nabla\right)\bar{\boldsymbol{\omega}}=\frac{\nabla\bar{p}\times\nabla\rho}{\rho^2}+\nu\nabla^2\bar{\boldsymbol{\omega}}+\nu_t\nabla^2\bar{\boldsymbol{\omega}}-\frac{2}{3}\nabla\times\left(\nabla k\right)-2\nabla\times\left(\boldsymbol{c}\times\bar{\boldsymbol{u}}\right) \tag{15}$$

where $\bar{\boldsymbol{\omega}}$ is the Reynolds-averaged vorticity. The Reynolds-averaged enstrophy transport equation can be obtained by taking the dot product between Eq. (15) and the Reynolds-averaged vorticity. The enstrophy transport equation is written as

$$\begin{aligned}\frac{\partial\left(\bar{\omega}_i\bar{\omega}_i/2\right)}{\partial t}&=\bar{\omega}_i\bar{S}_{ij}\bar{\omega}_j-\bar{u}_j\frac{\partial\left(\bar{\omega}_i\bar{\omega}_i/2\right)}{\partial x_j}+\frac{1}{\rho^2}\varepsilon_{ijk}\bar{\omega}_i\frac{\partial\rho}{\partial x_j}\frac{\partial p}{\partial x_k}\\&+\nu\frac{\partial^2\bar{\omega}_i}{\partial x_j\partial x_j}\bar{\omega}_i+\nu_t\frac{\partial^2\bar{\omega}_i}{\partial x_j\partial x_j}\bar{\omega}_i-\frac{2}{3}\varepsilon_{ijk}\frac{\partial^2 k}{\partial x_i\partial x_j}\bar{\omega}_k-2\left(\frac{\partial\left(c_i\bar{u}_j\right)}{\partial x_j}\bar{\omega}_i-\frac{\partial\left(c_i\bar{u}_j\right)}{\partial x_i}\bar{\omega}_j\right)\end{aligned} \tag{16}$$

$$G_\omega=\bar{\omega}_i\bar{S}_{ij}\bar{\omega}_j-\bar{u}_j\frac{\partial\left(\bar{\omega}_i\bar{\omega}_i/2\right)}{\partial x_j} \tag{17}$$

$$B_\omega=\frac{1}{\rho^2}\varepsilon_{ijk}\bar{\omega}_i\frac{\partial\rho}{\partial x_j}\frac{\partial p}{\partial x_k} \tag{18}$$

$$V_\omega=\nu\frac{\partial^2\bar{\omega}_i}{\partial x_j\partial x_j}\bar{\omega}_i \tag{19}$$

$$R_\omega=\nu_t\frac{\partial^2\bar{\omega}_i}{\partial x_j\partial x_j}\bar{\omega}_i-\frac{2}{3}\varepsilon_{ijk}\frac{\partial^2 k}{\partial x_i\partial x_j}\bar{\omega}_k \tag{20}$$

$$C_\omega=-2\left(\frac{\partial\left(c_i\bar{u}_j\right)}{\partial x_j}\bar{\omega}_i-\frac{\partial\left(c_i\bar{u}_j\right)}{\partial x_i}\bar{\omega}_j\right) \tag{21}$$

where $\bar{\omega}_i$ is the average vorticity, ε_{ijk} is the permutation symbol, and c_i is the angular velocity. G_ω is a relative vortex generation term, which accounts for the stretching and bending of vorticity owing to the velocity gradient. B_ω is a baroclinic torque term that represents the vorticity change caused by the non-parallel pressure gradient and the density gradient. Due to the incompressibility of the fluid, this term is ignored in this study. V_ω is the viscous term that represents the vorticity change due to the viscous effect of the fluid, R_ω is the Reynolds stress dissipation term, and C_ω is the Coriolis force term that is associated with the rotational motion of the impeller.[40,41]

The frequency domain characteristics of each item at the monitoring points on the blade's mean camber line for the impeller are analyzed using the FFT. Fig. 12 displays the frequency domain characteristics of the enstrophy transport equation at $0.8Q_{\mathrm{BEP}}$. As shown in the figure, the relative vortex generation term and the Reynolds stress dissipation term play a significant part in the vortex generation and dissipation processes, and the viscous term has the least influence. At $0.8Q_{\mathrm{BEP}}$, the relative vortex generation term G_ω, the Reynolds stress dissipation term R_ω, and the Coriolis force term C_ω exhibit the most intense pulsation on the pressure surface near the impeller shroud where the largest pulsation amplitude is distributed near the LE of the blade and extends to $\lambda = 0.6$. However, the viscous term V_ω exhibits the most intense pulsation amplitude on the suction surface. Near the suction surface, the maximum value of the pulsation amplitude is located at the TE of the blade, while at the middle of the flow channel and near the pressure surface, this maximum value is located at the LE of the blade. This indicates that, close to the impeller hub, unstable flow structures near the pressure surface are mainly affected by impeller inflow impingement. In contrast, the occurrence of flow separation in the TE region near the suction surface and the resulting generation of vortex flow is the main cause of unstable flow near the suction surface.

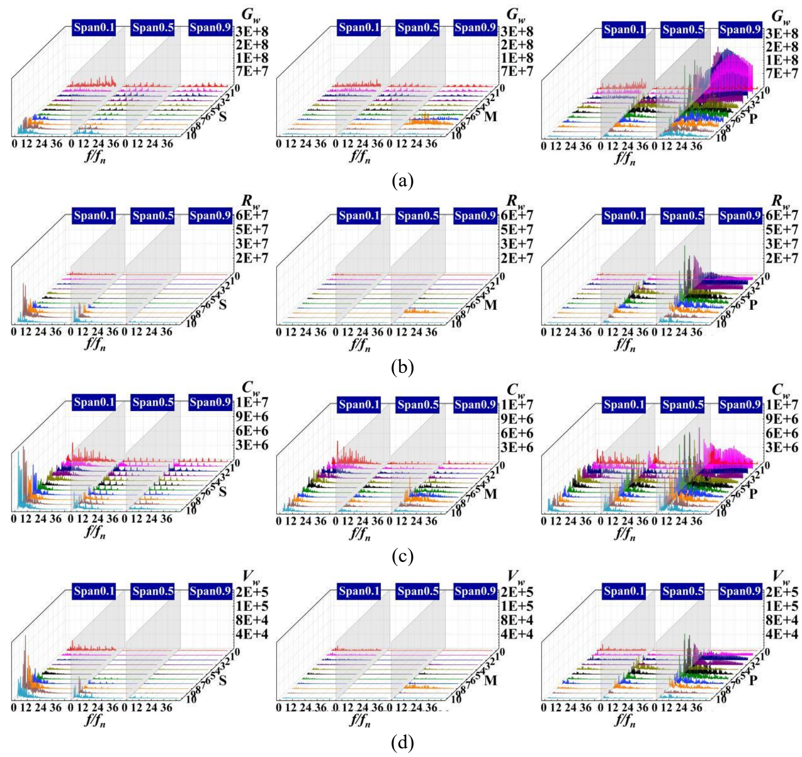

FIG. 12. Pulsation frequency domain of the transport equation of enstrophy at $0.8Q_{\mathrm{BEP}}$: (a) G_ω; (b) R_ω; (c) C_ω; (d) V_ω.

Fig. 13 shows the distribution of the components of the enstrophy transport equation at $0.8Q_{\mathrm{BEP}}$. Near the suction surface, the region with large values of the enstrophy transport equation is concentrated in the TE of the blade. Meanwhile, the region near the impeller hub is considerably affected by the wake of the guide vanes, leading to a high enstrophy region near the blade inlet that subsequently develops downstream. Near the impeller shroud, the high enstrophy region is generated near the pressure surface and develops along the flow direction.

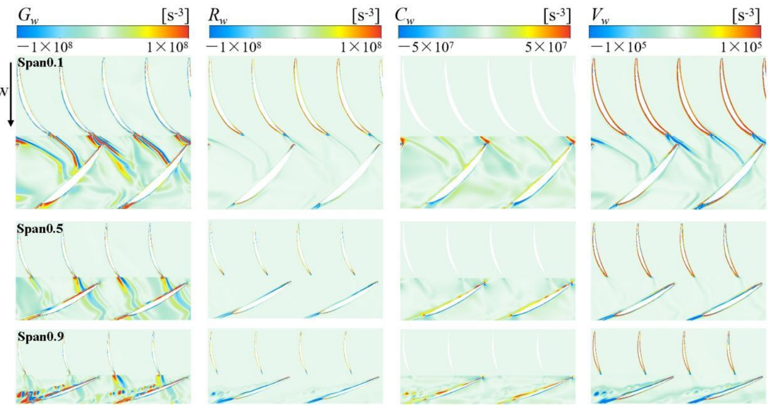

FIG. 13. Distribution on blade-to-blade surfaces at $0.8Q_{\mathrm{BEP}}$.

Fig. 14 displays the frequency domain characteristics of the enstrophy transport equation under optimum operating conditions. It is evident that the pulsation amplitudes of the enstrophy transport equation close to the suction surface are the most significant, and the region with the maximum pulsation amplitudes is concentrated at the TE of the blade. Meanwhile, the pulsation amplitudes of the enstrophy transport equation gradually decrease along the radial direction from the impeller hub to the shroud. As the suction surface profile becomes more curved closer to the hub, it results in a stronger swirling flow. In the middle of the flow channel and close to the pressure surface, the region with the largest pulsation amplitude is located at the blade inlet edge, and the amplitude gradually decreases along the flow direction.

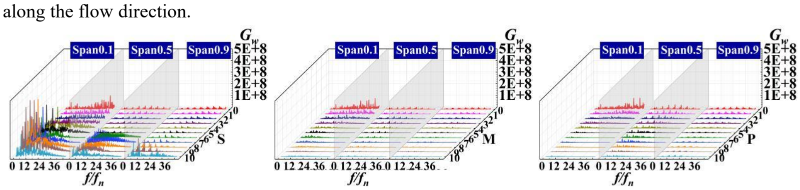

(a)

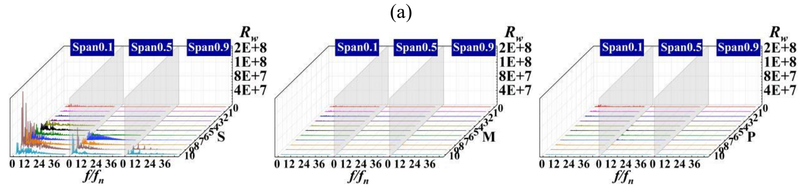

(b)

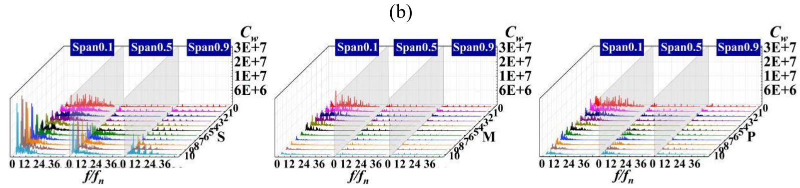

(c)

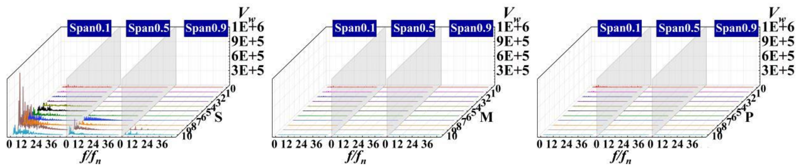

(d)

FIG. 14. Pulsation frequency domain of the enstrophy transport equation at Q_{BEP}: (a) G_ω; (b) R_ω; (c) C_ω; (d) V_ω.

Fig. 15 shows the distribution of the enstrophy transport equation under optimum operating conditions. Near the suction surface, the region with the large enstrophy amplitudes is mainly distributed at the TE of the blade. Near the impeller hub, enstrophy is considerably affected by the wake of the guide vanes, with a high enstrophy area forming near the blade inlet, which then develops downstream of the wake.

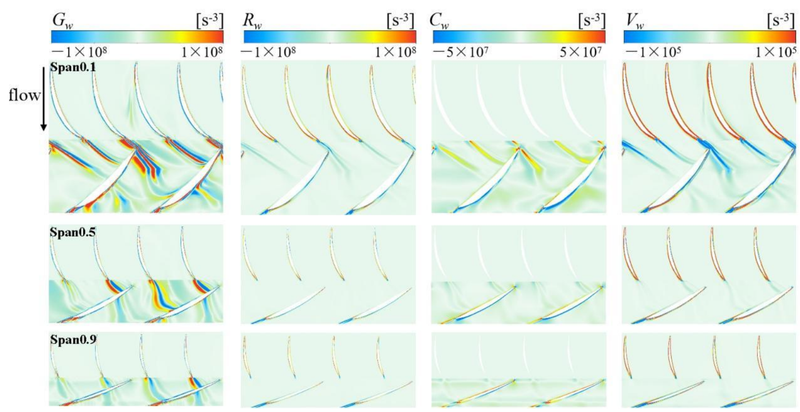

FIG. 15. Distribution on blade-to-blade surfaces at Q_{BEP}.

The frequency domain diagram of the enstrophy transport equation at $1.2Q_{\mathrm{BEP}}$ is shown in Fig. 16. Notably, the pulsation amplitudes of the enstrophy transport equation near the suction surface are the most significant, especially near the impeller shroud. At Span 0.5 and Span 0.9, the region where the pulsation is most intense is located at $\lambda = 0.3$. Near the hub, the pulsation amplitude is more evenly distributed along the flow direction. Compared to the suction surface, the pulsation amplitudes of the enstrophy transport equation in the middle of the flow channel and near the pressure surface are almost negligible.

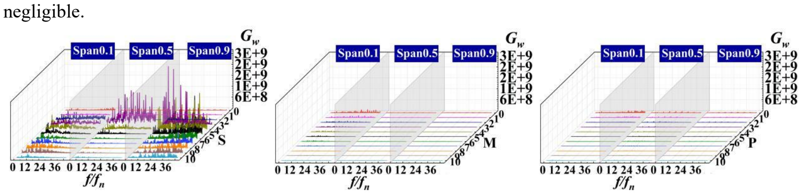

(a)

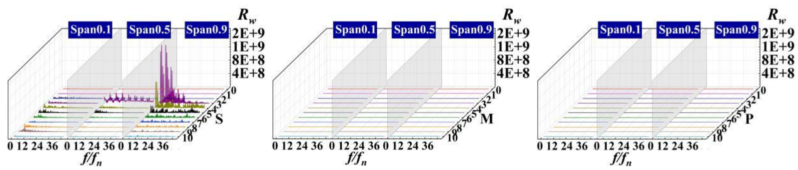

(b)

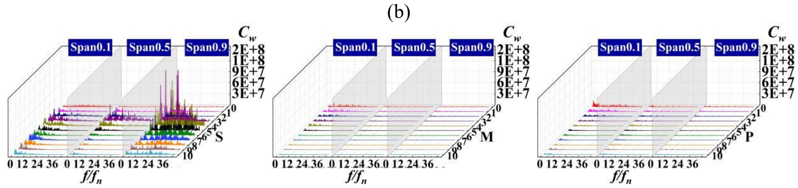

(c)

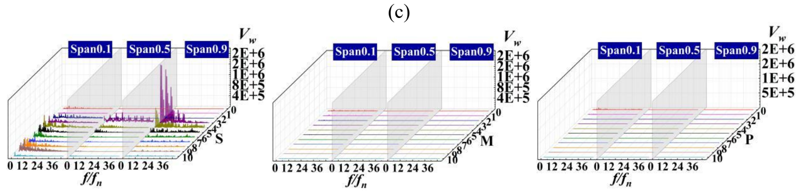

(d)

FIG. 16. Pulsation frequency domain of the transport equation of enstrophy at $1.2Q_{\mathrm{BEP}}$: (a) G_ω; (b) R_ω; (c) C_ω; (d) V_ω.

Fig. 17 shows the distribution of the enstrophy transport equation at $1.2Q_{\mathrm{BEP}}$. The relative vortex generation term and the Reynolds stress dissipation term are the main factors affecting vortex generation and dissipation. Meanwhile, near the impeller hub, which is more impacted by the wake of the guide vanes, the region with high values of enstrophy is formed near the blade inlet, which then develops downstream the wake to the neighboring blades. Near the impeller shroud, this high-enstrophy region is generated near the suction surface and develops along the flow direction.

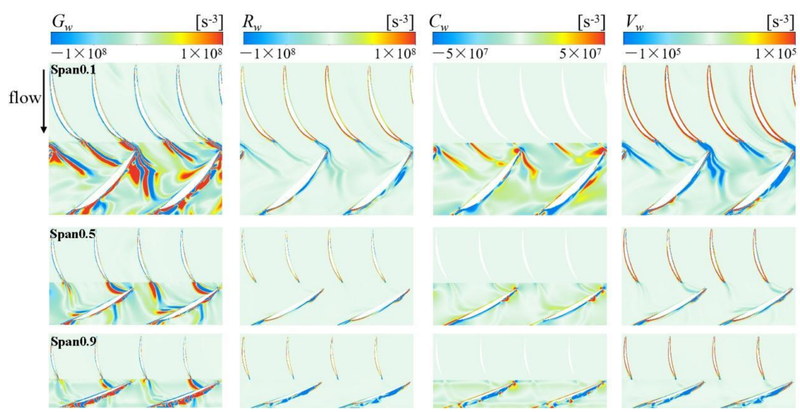

FIG. 17. Distribution on blade-to-blade surfaces at $1.2Q_{\mathrm{BEP}}$.

IV. CONCLUSIONS

In this study, numerical simulations of an axial flow PAT were performed to analyze different flow rate conditions close to the BEP. The flow instability of the PAT was investigated based on the relative streamline coordinate system. The following conclusions were drawn from the simulation results:

(1) Under off-design conditions, the mismatch between the relative inflow angle of the impeller and the blade inlet angle leads to impingement losses that generate an unstable flow near the LE of the blade. At low flow rate conditions, the impeller inflow impinges on the blade suction surface upon entering the LE of the blade. At high flow rate conditions, the impeller inflow impinges on the blade pressure surface, hindering smooth water flow into the impeller and causing a decrease in the relative velocity near the LE of the blade.

(2) The greater curvature of the suction surface profile leads to flow separation and vortex formation in the TE regions of the blade. Near the hub, the blade profile is more curved, and the maximum enstrophy in the flow direction is concentrated at the TE of the suction surface under all operating conditions. Under the optimum conditions, the maximum enstrophy at different span surfaces is focused on the TE of the suction surface, gradually decreasing along the radial direction from the impeller hub to the shroud. At low flow rate conditions, the maximum enstrophy is close to the pressure surface, while at high flow rate conditions, it is located near the suction surface.

(3) The unstable flow is generated near the LE of the blade under off-design conditions, resulting in significant pressure pulsations. Moreover, the unstable flow at the suction surface leads to larger amplitude pressure pulsations near the suction surface. In addition to the rotor-stator interference effects, the curvature of the blade suction surface profile and the bend structure of the inlet conduit are important factors affecting the distribution of pressure pulsations in the PAT.

(4) The relative vortex generation term and the Reynolds stress dissipation term play a significant role in both vortex generation and dissipation, while the viscous term has a lower effect. Regions with high amplitudes of the enstrophy transport equation are mainly distributed at the TE of the blade. In addition, in the impeller shroud, a region with large enstrophy amplitudes is generated close to the pressure surface at low flow rate conditions, while at high flow rate conditions, a large enstrophy amplitude region exists near the suction surface and develops downstream along the flow direction.

ACKNOWLEDGMENTS

This work was supported by the National Natural Science Foundation of China (52379086, 52009033), the Jiangsu Innovation Support Programme for International Science and Technology Cooperation (BZ2023047), the Postdoctoral Research Foundation of China (2022T150185; 2022M711021), and the Project on Excellent Post-graduate Dissertation of Hohai University (422003478).

AUTHOR DECLARATIONS

Conflict of Interest

The authors have no conflicts to disclose.

Author Contributions

Kan Kan: Conceptualization (lead); Formal analysis (equal); Funding acquisition (lead); Methodology (supporting); Resources (lead); Supervision (supporting); Writing - original draft (equal); Writing - review & editing (supporting). **Qingying Zhang:** Data curation (equal); Investigation (equal); Validation (lead); Writing - original draft (equal). **Jiangang Feng:** Methodology (equal); Resources (equal); Supervision (equal); Writing - review & editing (supporting). **Yuan Zheng:** Resources (supporting); Supervision (equal); Visualization (equal); Writing - review & editing (equal). **Hui Xu:** Resources (supporting); Supervision (equal); Visualization (equal); Writing - review & editing (equal). **Mosè Rossi:** Supervision (supporting); Visualization (equal); Writing - review & editing (equal). **Haoyu Li:** Data curation (equal); Formal analysis (equal); Methodology (supporting); Software (equal).

DATA AVAILABILITY

The data that support the findings of this study are available from the corresponding author upon reasonable request.

REFERENCES

[1]G. A. M. Castorino, L. Manservigi, S. Barbarelli, E. Losi, and M. Venturini, "Development and validation of a comprehensive methodology for predicting pat performance curves," Energy 274, 127366 (2023).

[2]M. Stefanizzi, T. Capurso, G. Balacco, M. Binetti, S. M. Camporeale, and M. Torresi, "Selection, control and techno-economic feasibility of pumps as turbines in water distribution networks," Renewable Energy 162, 1292-1306 (2020).

[3]M. H. S. Haghighi, S. M. Mirghavami, M. M. Ghorani, A. Riasi, and S. F. Chini, "A numerical study on the performance of a superhydrophobic coated very low head (VLH) axial hydraulic turbine using entropy generation method," Renewable Energy 147, 409-422 (2020).

[4]F. A. Plua, F. J. Sánchez-Romero, V. Hidalgo, P. A. López-Jiménez, and M. Pérez-Sánchez, "Variable speed control in PATs: theoretical, experimental and numerical modelling," Water 15(10), 1928 (2023).

[5]M. Tahani, A. Kandi, M. Moghimi, and S. D. Houreh, "Rotational speed variation assessment of centrifugal pump-as-turbine as an energy utilization device under water distribution network condition," Energy 213, 118502 (2020).

[6]K. Kan, Q. Zhang, Z. Xu, Y. Zheng, Q. Gao, and L. Shen, "energy loss mechanism due to tip leakage flow of axial flow pump as turbine under various operating conditions," Energy 255, 124532 (2022).

[7]H. Yu, T. Wang, Y. Dong, Q. Gou, L. Lei, and Y. Liu, "Numerical investigation of splitter blades on the performance of a forward-curved impeller used in a pump as turbine," Ocean Engineering 281, 114721 (2023).

[8]X. Li, T. Ouyang, Y. Lin, and Z. Zhu, " Interstage difference and deterministic decomposition of internal unsteady flow in a five-stage centrifugal pump as turbine," Physics of Fluids 35(4), 045136 (2023).

[9]Y. Zhang, W. Jiang, S. Qi, L. Xu, Y. Wang, and D. Chen, "Clocking effect on the internal flow field and pressure fluctuation of pat based on entropy production theory," Journal of Energy Storage 69, 107932 (2023).

[10]K. Kan, Z. Yang, P. Lyu, Y. Zheng, and L. Shen, "Numerical study of turbulent flow past a rotating axial-flow pump based on a level-set immersed boundary method," Renewable Energy 168, 960-971 (2021).

[11]M. Rossi, A. Nigro, and M. Renzi, "Experimental and numerical assessment of a methodology for performance prediction of pumps-as-turbines (PATs) operating in off-design conditions," Applied Energy 248, 555-566 (2019).

[12]M. Rossi, and M. Renzi, "A general methodology for performance prediction of pumps-as-turbines using artificial neural networks," Renewable Energy 128, 265-274 (2018).

[13]A. Telikani, M. Rossi, N. Khajehali, and M. Renzi, "Pumps-as-Turbines'(PATs) performance prediction improvement using evolutionary artificial neural networks," Applied Energy 330, 120316 (2023).

[14]A. Nasir, E. Dribssa, M. Girma, and H. B. Madessa, "Selection and performance prediction of a pump as a turbine for power generation applications," Energies 16(13), 5036 (2023).

[15]S. Yang, P. Li, Z. Lu, R. Xiao, D. Zhu, K. Lin, and R. Tao, "Comparative evaluation of the pump mode and turbine mode performance of a large vaned-voluted centrifugal pump," Frontiers in Energy Research 10, 1003449 (2022).

[16]T. Lin, Z. Zhu, X. Li, J. Li, and Y. Lin, "Theoretical, experimental, and numerical methods to predict the best efficiency point of centrifugal pump as turbine," Renewable Energy 168, 31-44 (2021).

[17]S. S. Yang, C. Wang, K. Chen, and X. Yuan, "Research on blade thickness influencing pump as turbine," Advances in Mechanical Engineering 6, 190530 (2014).

[18]J. Xu, L. Wang, S. Ntiri Asomani, W. Luo, and R. Lu, "Improvement of internal flow performance of a centrifugal pump-as-turbine (PAT) by impeller geometric optimization," Mathematics 8(10), 1714 (2020).

[19]M. Binama, W. T. Su, W. H. Cai, X. B. Li, A. Muhirwa, B. Li, and E. Bisengimana, "Blade trailing edge position influencing pump as turbine (PAT) pressure field under part-load conditions," Renewable Energy 136, 33-47 (2019).

[20]T. Wang, R. Xiang, H. Yu, and M. Zhou, "Performance improvement of forward-curved impeller with an adequate outlet swirl using in centrifugal pump as turbine," Renewable Energy 204, 67-76 (2023).

[21]R. Xiang, T. Wang, Y. Fang, H. Yu, M. Zhou, and X. Zhang, "Effect of blade curve shape on the hydraulic performance and pressure pulsation of a pump as turbine," Physics of Fluids 34(8), 085130 (2022).

[22]D. Adu, J. Zhang, M. Jieyun, S. N. Asomani, and M. O. Koranteng, "Numerical investigation of transient vortices and turbulent flow behaviour in centrifugal pump operating in reverse mode as turbine," Materials Science for Energy Technologies 2(2), 356-364 (2019).

[23]T. Xin, J. Wei, L. Qiuying, G. Hou, Z. Ning, W. Yuchuan, and C. Diyi, "Analysis of hydraulic loss of the centrifugal pump as turbine based on internal flow feature and entropy generation theory," Sustainable Energy Technologies and Assessments 52, 102070 (2022).

[24]Q. Si, J. He, S. Miao, J. Liu, A. Asad, and P. Wang, "Study on the energy conversion characteristics in the impeller of USSPAT based on velocity triangle space decomposition," Journal of Energy Storage 72, 108429 (2023).

[25]J. Hu, W. Su, K. Li, K. Wu, L. Xue, and G. He, "Transient hydrodynamic behavior of a pump as turbine with varying rotating speed," Energies 16(4), 2071 (2023).

[26]J. Yin, D. Wang, D. K. Walters, and X. Wei, "Investigation of the unstable flow phenomenon in a pump turbine," Science China Physics, Mechanics & Astronomy 57, 1119-1127 (2014).

[27]F. Zhang, D. Appiah, F. Hong, J. Zhang, S. Yuan, K. A. Adu-Poku, and X. Wei, "Energy loss evaluation in a side channel pump under different wrapping angles using entropy production method," International Communications in Heat and Mass Transfer 113, 104526 (2020).

[28]L. Ji, W. Li, W. Shi, F. Tian, and R. Agarwal, "Diagnosis of internal energy characteristics of

mixed-flow pump within stall region based on entropy production analysis model," International Communications in Heat and Mass Transfer 117, 104784 (2020).
[29]J. Zhang, D. Appiah, F. Zhang, S. Yuan, Y. Gu, and S. N. Asomani, "Experimental and numerical investigations on pressure pulsation in a pump mode operation of a pump as turbine," Energy Science & Engineering 7(4), 1264-1279 (2019).
[30]A. Meana-Fernández, J. M. Fernández Oro, K. M. Argüelles Díaz, M. Galdo-Vega, and S. Velarde-Suárez, "Application of Richardson extrapolation method to the CFD simulation of vertical-axis wind turbines and analysis of the flow field," Engineering Applications of Computational Fluid Mechanics 13(1), 359-376 (2019).
[31]X. Sun, G. Xia, W. You, X. Jia, S. Manickam, Y. Tao, S. Zhao, J. Y. Yoon, and X. Xuan, "Effect of the arrangement of cavitation generation unit on the performance of an advanced rotational hydrodynamic cavitation reactor," Ultrasonics Sonochemistry 99, 106544 (2023).
[32]X. Sun, W. You, X. Xuan, L. Ji, X. Xu, G. Wang, S. Zhao, G. Boczkaj, J. Y. Yoon and S. Chen," Effect of the cavitation generation unit structure on the performance of an advanced hydrodynamic cavitation reactor for process intensifications," Chemical Engineering Journal412, 128600 (2021).
[33]S. J. Daniels, A. A. M. Rahat, G. R. Tabor, J. E. Fieldsend, and R. M. Everson, "Shape optimisation of the sharp-heeled Kaplan draft tube: performance evaluation using computational fluid dynamics," Renewable Energy 160, 112-126 (2020).
[34]L. Ji, W. Li, W. Shi, F. Tian, amd R. Agarwal, "Effect of blade thickness on rotating stall of mixed-flow pump using entropy generation analysis," Energy 236, 121381 (2021).
[35]L. Ji, W. Li, W. Shi, H. Chang, and Z. Yang, " Energy characteristics of mixed-flow pump under different tip clearances based on entropy production analysis," Energy 199, 117447 (2020).
[36]D. Zhang, W. Shi, D. Pan, and M. Dubuisson, "Numerical and experimental investigation of tip leakage vortex cavitation patterns and mechanisms in an axial flow pump," Journal of Fluids Engineering 137(12), 121103 (2015).
[37]S. K. Ghai, N. Chakraborty, U. Ahmed, and M. Klein, "Enstrophy evolution during head-on wall interaction of premixed flames within turbulent boundary layers," Physics of Fluids 34(7), 075124 (2022).
[38]Y. Liu, X. Li, W. Wang, L. Li, and Y. Huo, "Numerical investigation on the evolution of forces and energy features in thermo-sensitive cavitating flow," European Journal of Mechanics-B/Fluids 84, 233-249 (2020).
[39]T. Yu, Z. Shuai, X. Wang, J. Jian, J. He, W. Li, and C. Jiang, " Research on wake and potential flow effects of rotor-stator interaction in a centrifugal pump with guided vanes," Physics of Fluids 35(3), 037107 (2023).
[40]K. Kan, Y. Xu, H. Xu, J. Feng, and Z. Yang, "Vortex-Induced energy loss of a mixed-flow waterjet pump under different operating conditions," Acta Mechanica Sinica 39(9), 323064 (2023).
[41]A. Kazbekov, K. Kumashiro, and A. M. Steinberg, "Enstrophy transport in swirl combustion," Journal of Fluid Mechanics 876, 715-732 (2019).